J. Fluid Mech. (2008), *vol.* 612, *pp.* 81–105.
doi:10.1017/S0022112008002838 Printed in the United Kingdom

Turbulent spot flow topology and mechanisms for surface heat transfer

D. R. SABATINO[1] AND C. R. SMITH[2]

[1]United Technologies Research Center, East Hartford, CT 06108, USA

[2]Department of Mechanical Engineering and Mechanics, Lehigh University, Bethlehem, PA 18015, USA

(Received 16 August 2007 and in revised form 7 June 2008)

The properties of artificially initiated turbulent spots over a heated plate were investigated in a water channel. The instantaneous velocity field and surface Stanton number were simultaneously established using a technique that combines particle image velocimetry and thermochromic liquid crystal thermography. Several characteristics of a spot are found to be similar to those of a turbulent boundary layer. The spacing of the surface heat transfer streak patterns within the middle or 'body' of a turbulent spot are comparable to the low-speed streak spacing within a turbulent boundary layer. Additionally, the surface shear stress in the same region of a spot is also found to be comparable to a turbulent boundary layer. However, despite these similarities, the heat transfer within the spot body is found to be markedly less than the heat transfer for a turbulent boundary layer. In fact, the highest surface heat transfer occurs at the trailing or calmed region of a turbulent spot, regardless of maturity. Using a modified set of similarity coordinates, instantaneous two-dimensional streamlines suggest that turbulent spots entrain and subsequently recirculate warm surface fluid, thereby reducing the effective heat transfer within the majority of the spot. It is proposed that energetic vortices next to the wall, near the trailing edge of the spot body, are able to generate the highest surface heat transfer because they have the nearest access to cooler free-stream fluid.

1. Introduction

Turbulent spots continue to draw research interest because they are a prominent element in naturally occurring transitional boundary-layer flows. They are of particular interest in gas turbine applications, where transitional flows on turbine airfoils are common and predicting the heat transferred to the airfoil is of great importance. Turbulent spots also provide a spatially limited patch of turbulence, which has the promise of containing the same types of structures as present in a fully turbulent boundary layer, but is more accessible to examination.

Gad-El-Hak, Blackwelder & Riley (1981) established some general characteristics of spots that continue to provide a common reference. Based on flow visualization, the authors described the spot as being comprised of several distinct regions. Figure 1 shows that the leading edge is elevated from the surface and overhangs the undisturbed laminar fluid very near the surface. This region is followed by what is best described as the 'body' of the spot, which appears to have the most active turbulent behaviour. Finally, the trailing or 'calmed' region of the spot includes the transition back to

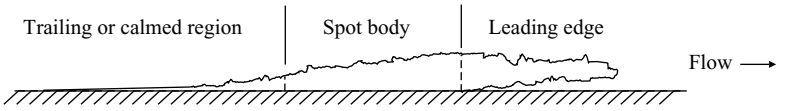

FIGURE 1. Schematic of a turbulent spot after Gad-El-Hak *et al.* (1981).

laminar conditions. The interface between the turbulent body and calmed region is often described as the 'trailing edge' of the spot.

The leading-edge overhang region has been explained by Gutmark & Blackwelder (1987) as upstream turbulence initially closer to the wall that was ejected into the far field. This description is very consistent with the process of turbulent boundary-layer growth and regeneration described by Smith (1996).

The body of the spot has received most of the research attention. Early flow measurements suggested that spots were dominated by primarily spanwise vortices (Wygnanski, Sokolov & Friedman 1976; Cantwell, Coles & Dimotakis 1978), but visualizations revealed a more complex structure that included many streamwise streak-like patterns (Cantwell *et al.* 1978; Gad-El-Hak *et al.* 1981; Perry, Lim & Teh 1981). Sankaran, Sokolov & Antonia (1988) measured the existence of multiple coherent structures and proposed that these were 'hairpin' type vortices. Yaras (2007) and Schröder & Kompenhans (2004) made spanwise velocity measurements parallel and normal to the wall and found evidence of hairpin vortices along with patterns of low and high streamwise velocity fluid or 'low-speed streaks.' Similarly, Zhong *et al.* (1999), examining surface heat transfer data, describe streak-like patterns comparable to those found in turbulent boundary layers. The presence of streamwise vortices has also been reported in direct numerical simulation (DNS) results, with Singer (1996) noting their influence on fluid entrainment under the leading-edge overhang, and Krishnan & Sandham (2007) finding these vortices were probably responsible for the lateral growth at the interface with the surrounding laminar fluid.

The trailing or calmed region of the spot is characterized by a velocity profile much fuller than the laminar profile, indicating the presence of higher momentum fluid near the wall (Antonia *et al.* 1981; Wygnanski, Zilberman & Haritonidis 1982; Gostelow *et al.* 1997; Chong & Zhong 2006). This key characteristic has been captured by a theoretical model proposed by Brown & Smith (2005). Additionally, the visualizations of Cantwell *et al.* (1978) reveal streamwise streak patterns within the calmed region that are more regular and have a higher aspect ratio than those found within the turbulent body of the spot. When Schröder & Kompenhans (2004) measured the flow field, they found that low-speed streaks in the spot, which extended into the calmed region, are associated with organized packets of hairpin vortices, as has been described by Adrian, Meinhart & Tomkins (2000). Schröder & Kompenhans (2004) also note that the most dynamic region of hairpin activity is at the interface between the body and calmed region of the spot and may be the principal mechanism for turbulence generation. The results of Haidari & Smith (1994) and Singer & Joslin (1994) may offer support for this proposal as they found experimentally and numerically that a turbulent spot could be generated from a single hairpin vortex through a process of secondary vortex generation. This type of vortex interaction and generation has been theoretically modelled using a new velocity–vorticity formulation by Bowles, Davies & Smith (2003).

The surface heat flux below turbulent spots has been directly measured by Clark, Jones & LaGraff (1994), Ching & LaGraff (1995) and de Lange, Hogendoorn & Steenhoven (1998). All three studies, performed in air, found that the maximum heat

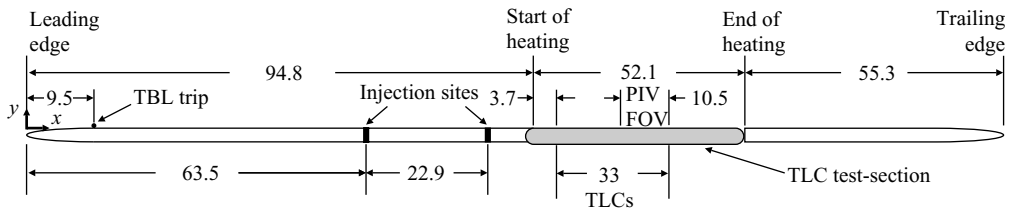

FIGURE 2. Elevation of experimental arrangment (all dimensions in cm). The PIV field of view was located on the injection site centreline ($z = 0$).

transfer levels achieved within the spot are comparable to those of an equivalent turbulent boundary layer. However, Zhong *et al.* (2000) measured heat transfer levels in water that were lower than fully turbulent values. The results of de Lange *et al.* (1998) and Zhong *et al.* (2000) imply that the body of the spot is responsible for the maximum surface heat transfer and the calmed region of the spot has correspondingly little effect on surface heat transfer. However, it is difficult to establish a direct correlation between the flow field and the surface heat transfer. In fact, Clark *et al.* (1994) hypothesized from the results of Mautner & Van Atta (1986), who measured the highest shear stress near the spot trailing edge, that the highest heat transfer should also occur near the trailing edge of the turbulent body.

In related studies, Antonia *et al.* (1981) and Chong & Zhong (2006) experimentally measured the fluid temperature inside turbulent spots over a heated plate. Both studies found that the body of the spot is primarily comprised of warm fluid, relative to the laminar boundary layer, while the trailing region contained the coolest fluid near the wall. Krishnan & Sandham (2007) calculated a very similar temperature profile using a DNS calculation of a Mach 2 flow, which prompted them also to propose that the highest heat transfer should be expected near the trailing edge.

The objective of the present study is to examine in detail the flow field and complementary surface heat transfer of turbulent spots to establish how a spot influences the surface heat transfer. Both the surface heat transfer and shear stress are examined to quantitatively compare the characteristics of turbulent spots with a fully developed turbulent boundary layer. Similarity coordinates that extend the work of Cantwell *et al.* (1978) and Wygnanski *et al.* (1982) enable the comparison of both the flow and heat transfer characteristics for spots of different maturity.

2. Experimental apparatus

The experiments were conducted in a closed-circuit free-surface water channel with a 5 m long, 0.9 m wide and 0.4 m deep working section. The channel is capable of free-stream velocities of 0.01 to 0.4 m s^{-1}, maintains a spanwise uniformity of 2 % and has a free-stream turbulence intensity of 0.1 % (Acarlar & Smith 1987). As shown in figure 2, the experiments were conducted on an elevated flat plate with a 5:1 elliptical leading edge. Similar to Cantwell *et al.* (1978), Gad-El-Hak *et al.* (1981), and Zhong *et al.* (2000), turbulent spots were artificially introduced into a laminar boundary layer by means of a wall-normal fluid injection through a 0.8 cm hole. In this case, each spot was generated with a 0.5 ml injection with an average velocity of 19 cm s^{-1} (Sabatino 1998).

The flow field was recorded using a high image-density particle image velocimetry (PIV) system (Adrian 1991; Rockwell *et al.* 1993) and surface heat transfer measurements were simultaneously recorded using thermochromic liquid crystal (TLC)

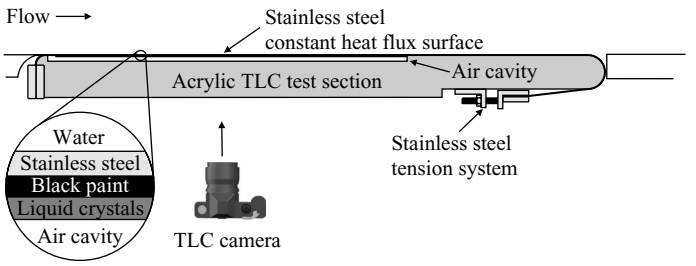

FIGURE 3. Thermochromic liquid crystal test-section details.

Case	x_i (cm)	U_∞ (cm s^{-1})	q (W m^{-2})	δ_i (cm)	δ_i^* (cm)	$(Re_x)_i$	$(Re_{\delta^*})_i$
1	86.4	16.0	5800	1.14	0.391	1.44×10^5	654
2	63.5	16.5	5800	0.96	0.320	1.09×10^5	568
3	63.5	22.0	5800	0.83	0.286	1.46×10^5	657
TBL	63.5	22.5	7949	2.17	0.271	1.49×10^5	635

TABLE 1. Turbulent spot and turbulent boundary layer (TBL) characteristic parameters. All data recorded at a free-stream temperature of 21.95 °C.

thermography described by Praisner, Sabatino & Smith (2001). The TLC test section (figure 3) consists of a thin (51 μm) stainless steel foil stretched across an acrylic plate, creating a sealed air-filled cavity with liquid crystals applied to the non-flow side and viewed from below through the polished acrylic test section. The coating on the under-surface of the foil is comprised of a layer of black paint (15 μm) and microencapsulated TLCs (40 μm), which provides a frequency response of more than 30 Hz (Praisner *et al.* 2001). A d.c. power supply connected to the stainless steel creates a constant heat flux surface and the liquid crystals are used to measure the surface temperature by carefully calibrating the hue, or primary wavelength of reflected light, to temperature across the entire LC coated surface (Sabatino 1998; Sabatino, Praisner & Smith 2001). The measured surface temperature is used to calculate the local surface heat transfer coefficient, h, which is presented non-dimensionally in the form of the Stanton number,

$$St = \frac{h}{c_p \rho U_\infty}. \tag{2.1}$$

As shown in figure 2, the PIV field of view (FOV) is located near the downstream edge of the heated surface. This location was selected to avoid the high heat flux region associated with the rapidly growing thermal boundary layer near the start of heating. The TLC coated area, also shown in the figure, depicts the streamwise extent of the surface heat transfer data that was recorded. The locations used to inject the fluid to initiate the turbulent spots along the centreline are also shown. Both PIV and TLC data were recorded on 36 exposure 35 mm film at 5 frames s^{-1}.

Turbulent spots of different 'maturities' were generated by varying both the free-stream velocity and the injection location, x_i. The injection boundary-layer thickness, δ_i, displacement thickness, δ_i^*, and corresponding Reynolds numbers are given for each case in table 1. Case 1 introduced a spot close to the field of view, with a relatively low free-stream velocity, and thus generated a young turbulent spot. The Case 2 flow velocity is similar to Case 1, but the injection location is further upstream and allows a longer development time, thus producing a more fully developed spot. Case 3

has a similar initial Reynolds number to Case 1, but the longer development time and higher velocity yield the most mature spot at the point of data acquisition. For comparison, data was also recorded for a turbulent boundary layer at a free-stream velocity similar to Case 3. The low-speed turbulent boundary layer was generated using a threaded rod boundary-layer trip near the flat-plate leading edge, as shown in figure 2. This type of low-Reynolds-number turbulent boundary layer, $Re_x \sim 1 \times 10^5$, has been shown to have turbulence characteristics similar to higher-Reynolds-number flows (Kim, Kline & Reynolds 1971; Purtell, Klebanoff & Buckley 1981; Smith & Metzler 1983) including velocity spectra (Lin & Rockwell 2001).

The heat flux levels in table 1, which were selected to use the entire measurable temperature range of the TLCs, minimize the uncertainty of the Stanton number. However, it was observed for Case 1 that the laminar boundary layer could exhibit buoyancy-induced instabilities if left undisturbed. This is confirmed by an examination of the ratio of the Gr_x/Re_x^2 which is approximately 1 for Case 1, where Gr_x is defined as:

$$Gr_x = \frac{g\beta(T_w - T_\infty)}{\nu^2}. \tag{2.2}$$

Here, β is the volumetric thermal expansion coefficient and T_w is the wall temperature. To prevent the buoyancy effects from influencing the results, the heating was applied, the spot was generated and the data were recorded before any instabilities could form.

3. Turbulent spot scaling

The measurement techniques employed in the present study provide relatively high spatial resolution, but low temporal resolution. Because the measurement areas are not large enough to capture the entire extent of a spot, a scaling technique is required in order to combine the discrete data sets so the entire spot behaviour can be examined. Additionally, an appropriate scaling is also required to enable meaningful comparisons between the different maturity spots.

Cantwell *et al.* (1978) proposed that the streamwise and vertical growth of a spot could be described using a conical similarity coordinate system.

$$\xi = \frac{(x - x_0)}{U_\infty(t - t_0)}, \tag{3.1}$$

$$\eta_c = \frac{y}{U_\infty(t - t_0)}. \tag{3.2}$$

Here x_0 and t_0 refer to the spatial and temporal location of the virtual origin of the spot growth, which is determined experimentally. The subscript applied to η simply distinguishes it from alternative scaling definitions presented below.

Cantwell *et al.* (1978) also described the following transformation for the calculation of the particle paths within a spot using the similarity coordinate system, which is invariant with the reference frame.

$$\xi' = \frac{u}{U_\infty} - \xi, \tag{3.3}$$

$$\eta' = \frac{v}{U_\infty} - \eta. \tag{3.4}$$

When ξ and η are defined by (3.1) and (3.2), respectively, they can be considered normalized bias velocities that produce a 'zoom' transformation to freeze the spot growth in the x and y directions.

Wygnanski *et al.* (1982) found that x_0 and t_0 could be effectively defined as the streamwise location and time of the spot generation. Wygnanski *et al.* (1982) found that the wall normal growth is proportional to the growth of a turbulent boundary layer with a momentum thickness at the spot generation location that matches the thickness of the laminar boundary layer at the same location.

$$\eta_w = \frac{y}{\delta_T}, \tag{3.5}$$

$$\delta_T = 0.37(x - x_s)^{4/5}\left(\frac{\nu}{U_\infty}\right)^{1/5}. \tag{3.6}$$

Here, δ_T is the momentum thickness of the turbulent boundary layer described above, and x_s is the streamwise offset used to set the thickness of the turbulent and laminar boundary layers equal at the point of injection. This model of the y growth of a spot is adopted for the present study. However, the form of (3.5) is not compatible with the transformation used to present invariant particle paths (3.4). Therefore, a new definition of η is proposed; this definition accounts for the Reynolds-number dependence included in (3.5) and can be used in the particle path transformation (3.4),

$$\eta = \frac{y}{\delta_T}\frac{\partial \delta_T}{\partial x}\frac{\partial x}{\partial t}\frac{1}{U_\infty} = \frac{4}{5}\frac{y}{x - x_s}\frac{x - x_0}{t - t_0}\frac{1}{U_\infty}. \tag{3.7}$$

The present study employs similarity coordinates based on (3.1) and (3.7), and assumes that t_0 and x_0 are identical to the injection time and streamwise location, respectively.

4. Laminar boundary layer

For each data acquisition sequence, the PIV data included several frames of the initial laminar boundary layer before the spot passed into the field of view. These initial data frames were used to establish a laminar boundary-layer reference from which to assess the turbulent spot activity. These initial data frames were averaged both spatially (in the streamwise direction) and temporally to provide a single profile representative of the initial laminar boundary layer prior to the passage of each spot (the height of the boundary layer changes 2 % over the PIV FOV). Figure 4 plots the initial boundary-layer profiles for all three spot cases using Blasius coordinates.

5. Surface heat transfer patterns

The surface heat transfer data are examined first to gain insight into the flow structure very near the surface and to compare qualitatively spot characteristics to a turbulent boundary layer. Figure 5 shows the instantaneous surface Stanton number behaviour for all three turbulent spot cases, as well as for the turbulent boundary layer. Each case is comprised of a temporal sequence of instantaneous Stanton number data that have been cropped to the same streamwise extent as the PIV field of view. The result is a composite view of the influence of the entire spot as it passes across the field of view; the time from injection is given below each data frame. Data were captured at 5 frames s^{-1}, but only every other frame is shown in figure 5 in order to display the entire temporal record. The Stanton number scale was uniquely

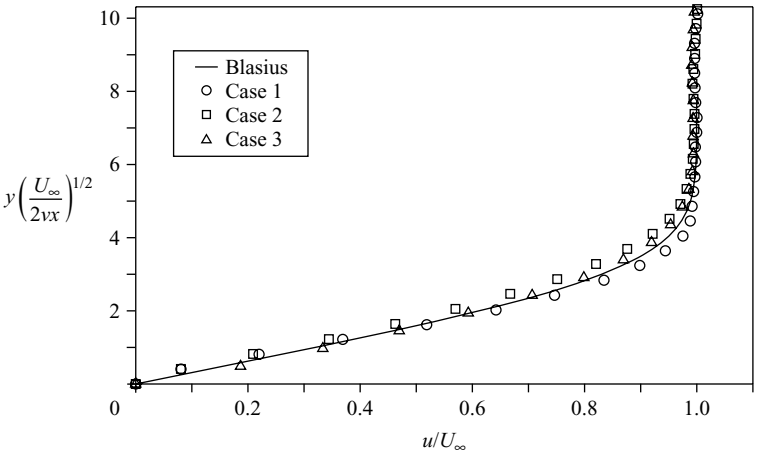

FIGURE 4. Initial laminar boundary-layer profile for all three turbulent spots.

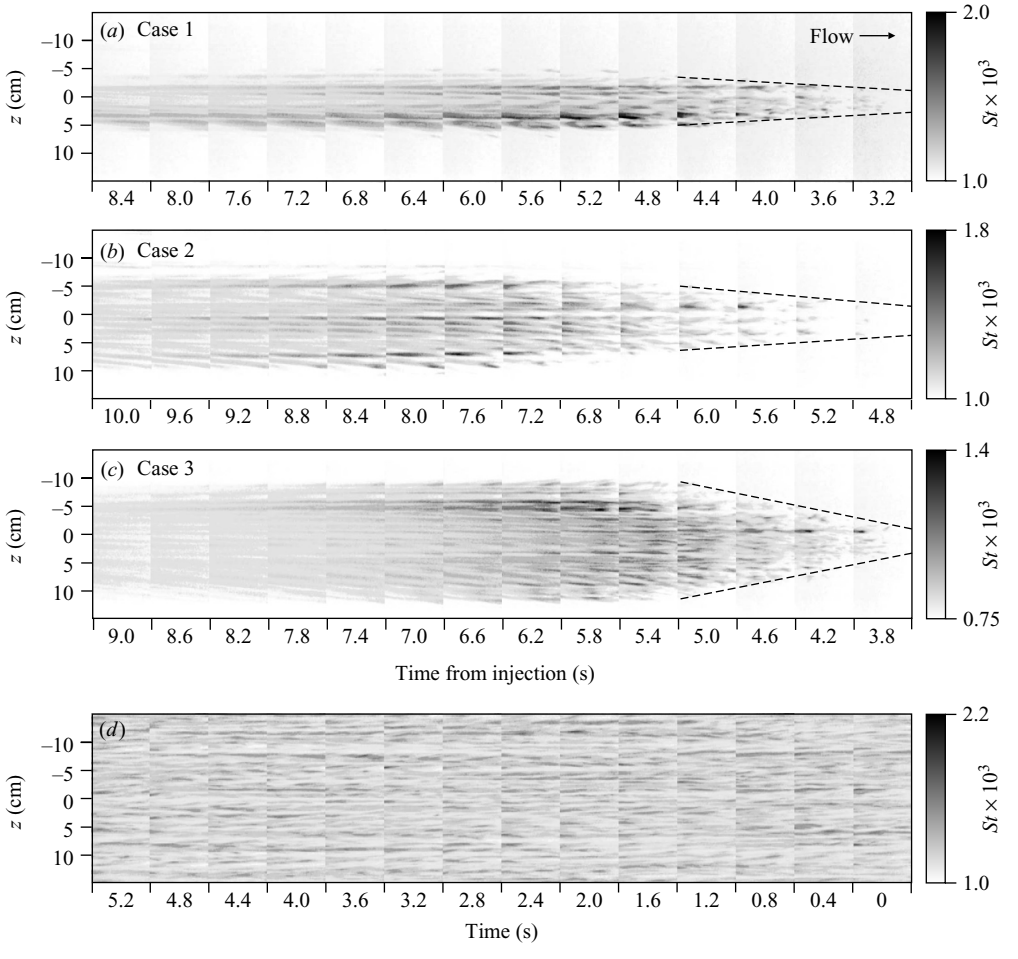

FIGURE 5. Temporal sequence of instantaneous Stanton number for (*a–c*) three turbulent spots and (*d*) a turbulent boundary layer.

selected for each case to provide the best visualization of the patterns. More precise quantitative comparisons will be made in subsequent sections.

Several notable features are apparent from figure 5. The prominent arrowhead leading edge identified with turbulent spots is clearly present for all three spot cases (Cantwell *et al.* 1978; Gad-El-Hak *et al.* 1981). The spanwise growth of the spot develops more rapidly as the spot matures. For comparative purposes only, the angle formed by the spanwise boundaries of the spot leading edge is noted with dashed lines. The rate of spanwise growth at the leading edge is correlated to the rate of spanwise decay at the trailing region of the spot. Therefore, the Case 3 spot has the most rapid spanwise growth at the leading edge, and the width of the spot at the trailing region decreases more rapidly than the other cases as the flow re-laminarizes.

The leading edges of the spots display a streamwise-oriented Stanton-number pattern, with somewhat organized spacing and moderate aspect ratio streaks (streamwise length/spanwise width). As time increases, and the spot grows in the spanwise direction, the Stanton number pattern elongates and changes to high-aspect-ratio streaks that are more closely spaced. Even at the most trailing portion of the spots, where the heat transfer levels are returning to those of the surrounding laminar boundary layer, the high-aspect-ratio pattern is visible.

The turbulent boundary layer shown in figure 5(*d*) was recorded at a free-stream velocity comparable to Case 3, and has an overall average Stanton number of 1.2×10^{-3}. The turbulent boundary-layer heat transfer generates a high-aspect-ratio pattern that is a result of the low-speed streaks that are characteristic of the near-wall region of turbulent boundary layers (Smith & Metzler 1983). The patterns can be seen to extend across multiple images, which suggests their streamwise persistence. Comparing figures 5(*c*) and 5(*d*), it is apparent that some portions of the turbulent spot display a Stanton-number pattern that is qualitatively similar to the low-speed streaks of the turbulent boundary layer.

To compare better the different maturity spots, the Stanton-number data are replotted in figure 6 using the streamwise similarity coordinate, ξ, as defined in (3.1). In figure 6, the leading edges of the data frames were cropped when the nonlinear streamwise scaling created overlap between frames. It is important to recognize that the streamwise similarity coordinate, ξ, can be interpreted as the speed of the structures within the turbulent spot relative to the free-stream velocity. For example, any identifiable patterns appearing at $\xi = 1.0$ in figure 6, would be assumed to be moving at the same velocity as the free stream. Accordingly, patterns appearing at lower values of ξ will be moving proportionately less than the free-stream velocity. The figure clearly shows that the first detectable change in heat transfer occurs near $\xi = 0.75$ for all three cases, suggesting that the velocity of the leading edge of the Stanton-number pattern is $0.75U_\infty$. It is also apparent that the scaling has the effect of making the arrowhead leading-edge angle much more consistent for all three cases. Finally, figure 6 qualitatively indicates that the maximum surface heat transfer occurs between $0.45 < \xi < 0.55$.

An examination of figures 5 and 6 suggests a change in the aspect ratio in the patterns from the leading to trailing regions of the spot. To examine this transition, selected Stanton-number frames which include data beyond the boundaries of the PIV field of view are shown in figure 7. The data are plotted versus non-dimensional time, T, so that the physical aspect ratio is preserved; however, ξ values are shown for reference on the second scale,

$$T = \frac{1}{\xi} = \frac{U_\infty (t - t_0)}{(x - x_0)}. \tag{5.1}$$

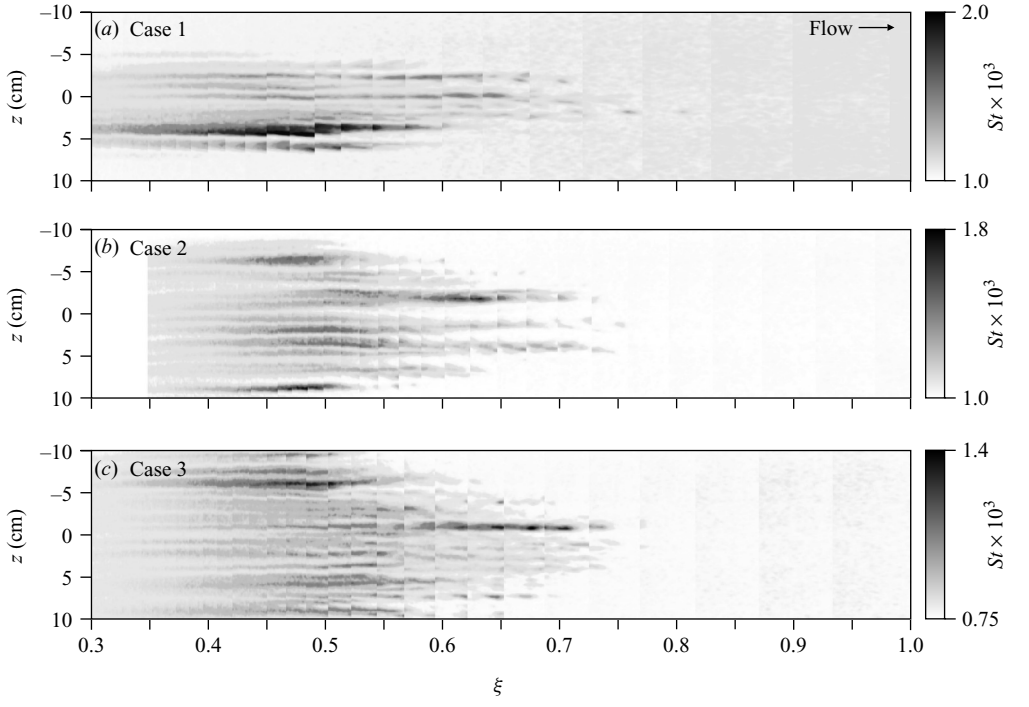

FIGURE 6. Surface Stanton number as a function of the streamwise similarity coordinate.

In all three cases, the Stanton-number pattern reveals low-aspect-ratio streaks near the angled leading edge. From direct observation, these low-aspect-ratio patterns are found to be temporally and spatially unsteady, suggestive of turbulent activity. Moving upstream, the pattern changes ($\xi \approx 0.5$) to higher-aspect-ratio streaks that persist beyond the edge of the frame. In contrast to the leading edge, these high-aspect-ratio patterns at the upstream edge of each frame persist spatially and temporally, as evidenced by the patterns in figures 5 and 6.

As the spot maturity increases from Case 1 to Case 3, the location of the pattern transition appears more prominent. In fact, the interface between the low and high heat transfer regimes in figure 7(*c*) is comparable to the transition between the highly turbulent patterns observed within a spot to the long streaks within the calmed region as visualized by Cantwell *et al.* (1978) and Gad-El-Hak *et al.* (1981). It is noted that the ξ values that characterize this transition in Stanton-number pattern generally coincide with the higher levels of heat transfer apparent from figure 6.

Further, the streak patterns of the Case 3 spot are qualitatively comparable to those observed in the turbulent boundary layer in figure 7(*d*). In particular, the Case 3 Stanton-number patterns near the transition from low- to high-aspect-ratio streaks appear to be most similar to the streaks within the turbulent boundary layer. However, despite the similarity in patterns, the maximum Stanton number for the turbulent boundary layer is approximately 1.5 times greater than the maximum Stanton number for the comparable Case 3 turbulent spot. Providing an explanation for this observation is one of the objectives of the present study, and a discussion follows in § 6.

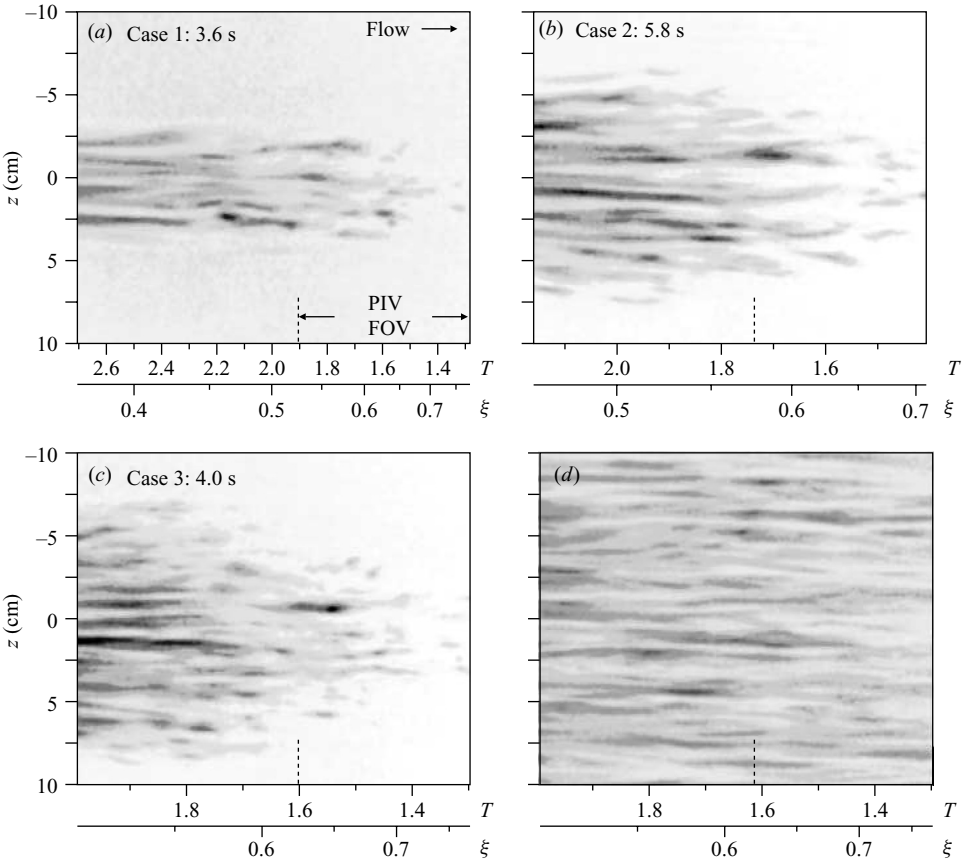

FIGURE 7. (*a–c*) Single-frame Stanton-number patterns for turbulent spots and (*d*) turbulent boundary layer. The time from injection is given and the PIV field of view is noted for reference. Stanton-number scales as in figure 5.

6. Combined flow field and surface heat transfer data

To understand how the velocity field behaviour relates to the surface Stanton-number patterns, the PIV data were used to generate instantaneous streamlines in similarity coordinates, (3.3) and (3.4). As previously noted, Cantwell *et al.* (1978) describes the use of these similarity coordinates as a 'zoom' transformation that freezes the growth of the spot in both the x and y directions, thus eliminating the time dependence of the streamlines. This transformation enables the fluid motion of the entire spot to be displayed on a single plot, even though the data set contains temporally discrete, spatially limited measurements of a passing spot.

Because similarity coordinate streamlines can produce non-intuitive patterns, figure 8 is included to show examples of both a uniform flow field and a laminar boundary layer as references. The uniform flow field shown in figure 8(*a*) reveals that all streamlines are directed toward $\xi = 1$. This pattern effectively shows how the reference frame is 'zooming' out in both the ξ and η directions. The laminar boundary layer, shown in figure 8(*b*), displays a generally similar pattern. However, instead of the lines converging at $\xi = 1$, they are directed upstream near the wall, marking the slower-moving fluid inside the boundary layer.

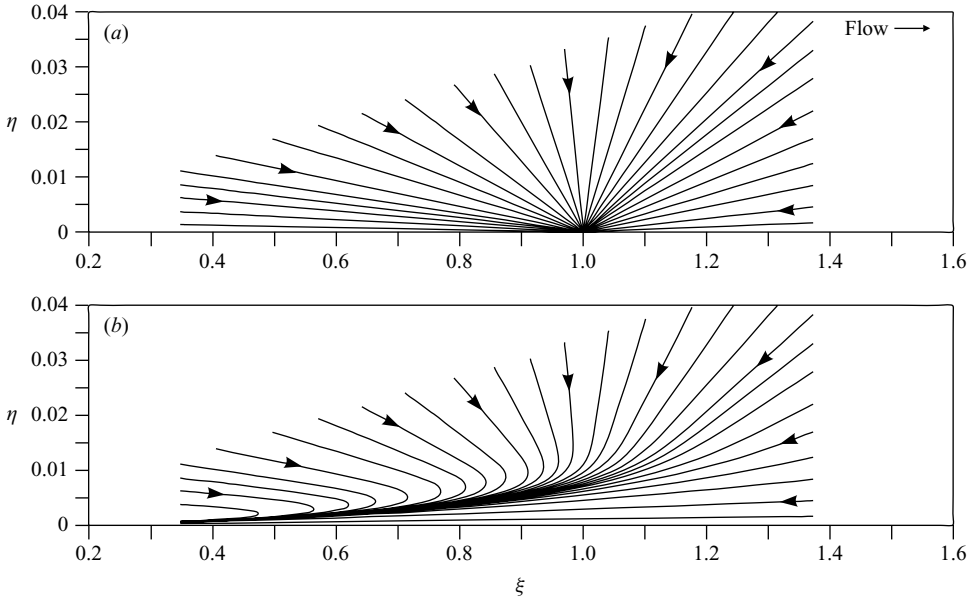

FIGURE 8. Similarity coordinate streamlines for a uniform flow field (*a*) and a Case 2 laminar boundary layer (*b*).

The flow-field and heat-transfer data for all three turbulent spots are presented in similarity coordinates in figure 9. The flow field is represented as both streamlines and velocity fluctuation level contours. The streamlines were calculated from a 'mosaic' velocity field assembled from scaled and cropped individual data frames, similar to the process used to create figure 6. For reference, the laminar boundary-layer thickness at both the leading and trailing edges of the frame is shown in figure 9 as grey bars. Arrows at the perimeter of the frame indicate the local flow direction and illustrate the direction of the flow within the entire spot. Recalling that the value of ξ can be interpreted as the velocity, relative to the free stream, of the structures within the spot at that coordinate location, the η coordinate in figure 9 represents the relative velocity of structures in the wall normal direction at that coordinate location.

Overlaid on the streamline patterns is a contour plot of the velocity fluctuation level, u'/U_∞, which is the variation of the streamwise velocity from the corresponding laminar boundary-layer velocity at the same wall normal location. Fluid moving more slowly than the initial laminar boundary-layer velocity is shown in blue, while fluid moving faster is shown in red. Directly below the flow-field data is the experimentally measured Stanton number along the injection centreline. These values are an average over 50 pixels, or 4 cm, in the spanwise direction. Because the Stanton number is a scalar, it was not necessary to crop the data in the streamwise direction, thus overlapping data are shown.

Examining the velocity fields for all three cases, there are several notable similarities. The streamlines indicate that the flow at the leading edge of the frames appears as relatively smooth streamlines that are directed toward the wall. This pattern reflects the characteristics of an undisturbed laminar boundary layer as illustrated in figure 8(*a*). The leading edges of the spots appear to be located in the range $0.9 < \xi < 1.0$ where the streamlines begin to suggest vortical patterns and there is a noticeable deficit in the velocity fluctuations (blue shading). These leading-edge structures are apparently

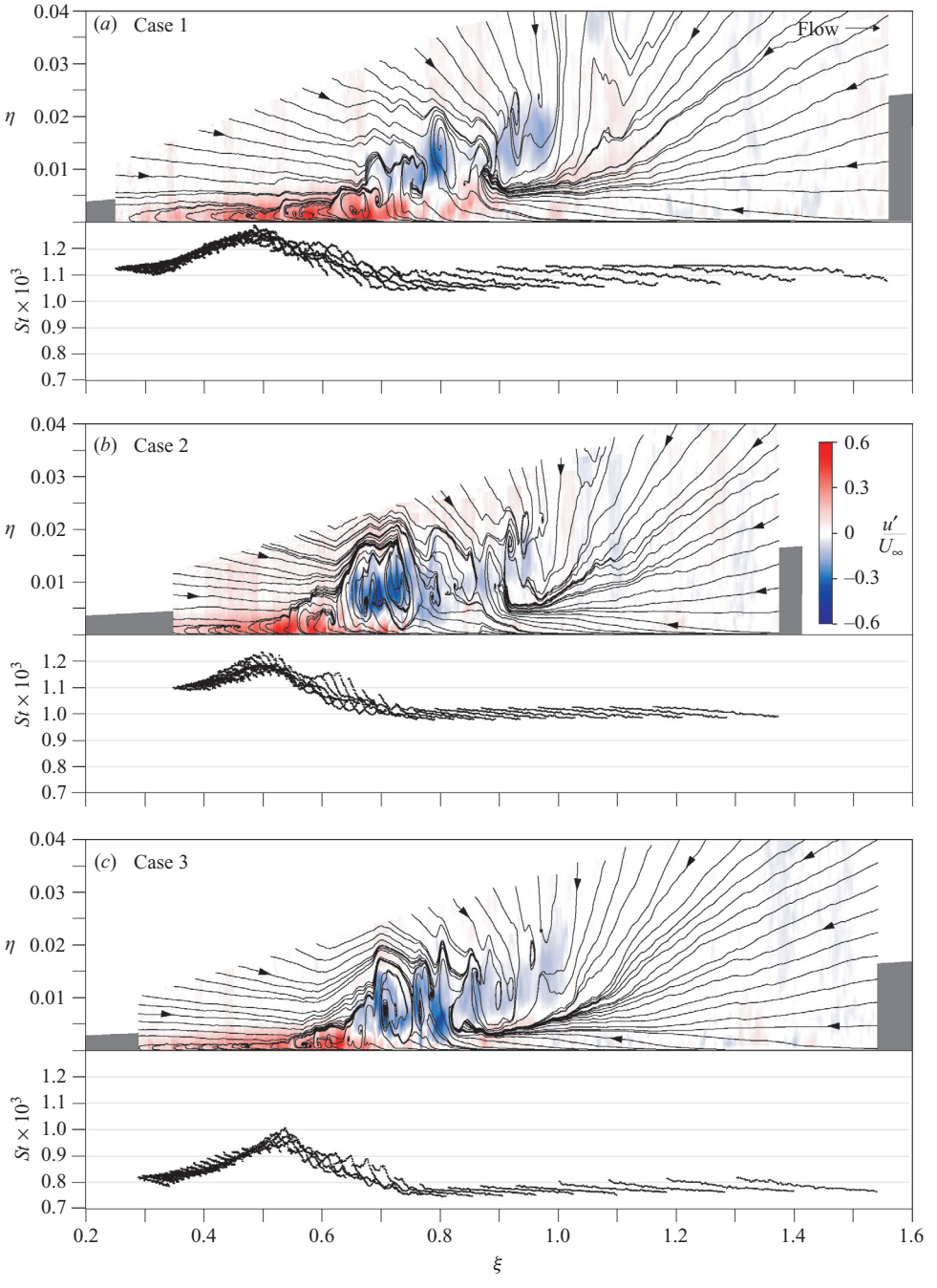

FIGURE 9. Similarity coordinate streamlines, laminar velocity fluctuation and corresponding centreline surface heat transfer. The laminar boundary-layer height is shown as grey bars at the leading and trailing edges of the frame.

entraining slower-moving fluid from near the surface, as indicated by the streamlines moving upstream and away from the surface. The largest negative velocity fluctuations occur in the range $0.6 < \xi < 0.8$, which suggests that this region encompasses the body

of the spot based on the description of Gad-El-Hak *et al.* (1981). This region is also characterized by vortical streamline patterns that appear to be entraining slower near-wall fluid from directly below the vortices, and faster-moving fluid from the free stream, with a resultant mixing of these two entrained streams. The streamlines from the far field in this region generally direct flow toward the energetic vortical structures within the spot, but do not appear to direct flow toward the wall itself. Finally, the trailing edge of the spot appears to be located near $\xi = 0.6$, where the closed streamline patterns cease and the velocity fluctuation contours indicate a strong increase (red shading) near the wall, apparently marking the calmed region.

Focusing on the surface Stanton-number patterns for $\xi > 1.1$, the individual Stanton-number profiles display a monotonically decreasing trend with increasing ξ. This trend is due to the change in the thermal boundary-layer thickness in the streamwise direction over the PIV field of view. In general, the spot activity does not appear to have a significant impact on the surface heat transfer until $\xi < 0.7$. This is consistent with figure 6, which confirms that the heat transfer across the entire span of the test surface also remains at initial conditions for $\xi > 0.75$. This finding is in strong contrast with the increased activity in the flow field directly above. Within the region $0.3 < \xi < 0.75$, the Stanton-number patterns show a marked increase and eventual peak near $\xi = 0.5$ in what appears to be the calmed region of the spot. The Case 1 spot has a Stanton-number peak that is approximately 16 % greater than the reference laminar boundary-layer value. The peak increase in the Stanton number beyond the laminar levels is, respectively, 21 % for Case 2 and 28 % for Case 3.

Based on the data of figure 9, some general observations can be made. First, it is notable that although the streamlines are based on two-dimensional instantaneous velocity fields, the general similarity of the streamline patterns within all three spot cases suggests that they provide a meaningful representation of generic spot behaviour. That the features within the spot patterns occur at similar ξ values is also validation of the selected scaling parameters.

From the Stanton-number data, it is clear that the overhang region at the spot leading edge has little influence on the surface heat transfer owing to the distance the flow structure is removed from the surface. However, more interesting is that the large energetic structures comprising the body of the spot also have minimal influence on surface heat transfer. Gutmark & Blackwelder (1987) describe the spot overhang as decaying ejected former near-wall turbulence, whereas the structures that comprise the spot body are described as energetic structures that are removed from, but still in proximity of, the surface. Similar to the flow structures within a turbulent boundary layer, which stimulate the generation of new vorticity near the surface and then propagate away from the wall (Smith 1996), it seems that the flow structures comprising the body of the spot may be the remnants of near-wall activity, and their usefulness for influencing surface heat transfer may be diminished. Additionally, Antonia *et al.* (1981), Gutmark & Blackwelder (1987), Sankaran *et al.* (1988), Chong & Zhong (2006) and Krishnan & Sandham (2007) all determined that only the most near-wall fluid comprising the body of the spot has a temperature elevated above that of a laminar heated boundary layer. This suggests that the spot is most probably comprised of an accumulation of warm fluid, the source of which is ejections of heated surface fluid, stimulated by these energetic spot body structures. Because the spot body temperature is elevated, the temperature gradient between the surface and the body of the spot is reduced as is the opportunity for increased heat transfer.

Examining the trailing region, the velocity fluctuation contours show that this area displays a strong inflow of fluid near the surface, immediately following the passage

of the body of the spot. However, examination of the associated wall normal velocity fluctuations, v', in the same region suggests no significant differences from a laminar flow, indicating that a three-dimensional flow pattern must be supplying the observed flow. Schröder & Kompenhans (2004) found that the trailing-edge region contains a large number of Q4 or 'sweep' events, which bring higher-momentum fluid to the surface and are evidence of hairpin vortices. These structures are highly three-dimensional, and would cause Q4 events that would be difficult to capture by the symmetry plane PIV employed in the current study. Additionally, the Stanton-number images shown in figure 7 suggest that this calmed region is composed of persistent streaks that do not appear to be turbulent in nature. It is therefore hypothesized that hairpin vortex packets near the trailing edge of the spot initially generate these streak patterns that, without additional vortex interaction, simply decay in the stable calmed region as discussed in § 5. It is relevant to note that Antonia *et al.* (1981), Chong & Zhong (2006) and Krishnan & Sandham (2007) all found that the calmed region just upstream of the body of the spot contains the coolest fluid within the spot, and therefore offers the best opportunity for heat transfer. Combining these findings with those of the current study make it possible to propose that hairpin vortex packets at the leading edge of the calmed region enable an inrush of cooler fluid to the surface and thus generate the peak surface heat transfer.

As described above, the percentage difference in the peak Stanton number owing to passage of the spot (relative to the initial laminar boundary layer) increases with spot maturity. Close examination of the trailing region for the three spots shown in figure 9 indicates that the thickness of the calmed region decreases from Case 1 to Case 3, as evidenced by the reduction in the extent of the positive u' region (red shading). This reduction in thickness may suggest that the cooler free-stream fluid migrates closer to the surface as a spot matures, resulting in consequently higher surface heat transfer. The peak heat transfer level of Case 3 is approximately 80 % of the average heat transfer for the comparable turbulent boundary layer as reported in § 5. This increase appears to be consistent with the results of Zhong *et al.* (2000), who also measured turbulent spots in water. However, this increase is lower than the peak heat transfer found by Clark *et al.* (1994) and de Lange *et al.* (1998), whose experiments in air measured spots with peak levels comparable to average levels in turbulent boundary layers. This discrepancy is probably a result of the difference in Prandtl numbers between the air and water experiments.

To investigate further whether the current findings are consistent with previous work, the speeds of the spot features were directly calculated. In this case, the speed of the velocity and Stanton-number fluctuations were established from instantaneous isocontours and are plotted in figure 10 for all three spots. The isocontours used to determine the speeds were selected as the smallest fluctuation level that could be reliably tracked between data frames.

Figure 10 shows the velocity fluctuation isocontour, $u'/U_\infty = 0.08$, has essentially the same speed, $0.9U_\infty$, for all three spots. Figure 9 illustrates that identification of the leading edge is subjective and that values ranging from $0.9U_\infty$ to $1.0U_\infty$ are possible. However, the speed shown in figure 10 is consistent with several previous studies which also used a threshold technique to establish the speed of the velocity fluctuations (Wygnanski *et al.* 1976; Cantwell *et al.* 1978; Gutmark & Blackwelder 1987).

The leading-edge speed of the Stanton-number fluctuation is significantly slower, as is expected based on the discussion of figure 9. Although this is different from the velocity-fluctuation speed, similar results have been reported by previous workers. Clark *et al.* (1994) and Ching & LaGraff (1995) directly measured the surface heat

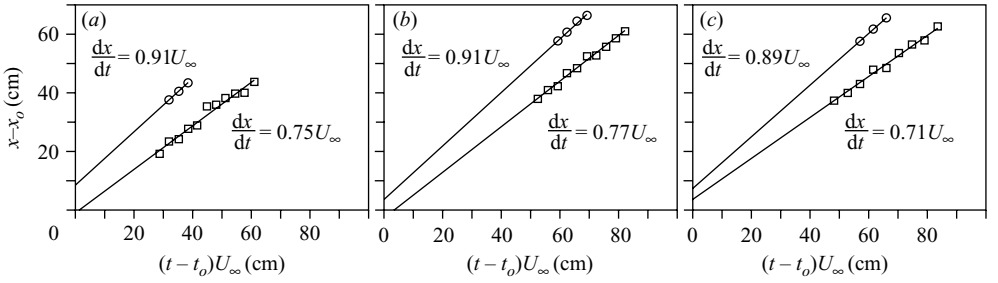

FIGURE 10. Leading-edge speed of isocontours based on velocity (○) and Stanton-number (□) fluctuation levels. Velocity isocontour: $u'/U_\infty = 0.08$. Stanton-number isocontours: (*a*) Case 1, 1.19×10^{-3}; (*b*) Case 2, 1.09×10^{-3}; (*c*) Case 3, 0.85×10^{-3}.

flux of passing spots and reported a leading-edge speed of the heat transfer as low as $0.81U_\infty$. Further, Clark *et al.* (1994) and Ching & LaGraff (1995) also found that the peak heat transfer is between $0.48U_\infty$ and $0.56U_\infty$, which is consistent with the peak at $\xi \approx 0.5$ in figure 9. In contrast, the heat-transfer measurements of de Lange *et al.* (1998) and Zhong *et al.* (2000) imply the leading and trailing edges of the heat transfer coincide with the leading and trailing edges of the flow structures within the spot. However, Zhong *et al.* (2000) reported the leading-edge speed of the heat-transfer fluctuations to be $0.78U_\infty$ and, when the data is replotted in similarity coordinates, the peak surface-heat transfer speed is in the range $0.5 < \xi < 0.6$.

7. Turbulent boundary-layer flow field

The streamline patterns for the turbulent spots shown in figure 9 suggest that the cooler free-stream fluid entrained by the body of the spot does not penetrate to the surface, thus resulting in a small heat-transfer increase despite elevated fluid activity within the body. However, the similarity between the surface Stanton-number patterns for the three turbulent spot cases and the turbulent boundary, shown in figures 5 and 7, raises the question of how similar the flow processes are within a turbulent spot and a turbulent boundary layer. To examine this question, the streamlines in similarity coordinates are compared for the Case 3 turbulent spot (figure 11*a*) and the turbulent boundary layer (figure 11*b*). The calculated turbulent boundary-layer thickness for the tripped turbulent boundary layer was used in the definition of η, (3.7). To make the ξ-axis compatible with the turbulent spot, the Case 3 injection time and location were also used to plot the turbulent boundary layer. Although this is an artificially imposed scaling, the turbulent boundary layer contains many scales of coherent structures convecting at different velocities and the use of this similarity scaling simply provides a means for comparing the same scale/speed structures to those at a particular location within a turbulent spot.

Figure 11 shows a general pattern of vortical structures, within both the spot and the turbulent boundary layer, that appear to entrain fluid from both upstream and downstream. However, the strong vortical streamline patterns evidenced within the turbulent spot are not nearly as pronounced within the turbulent boundary layer. The vortical patterns are pronounced only when the frame of reference velocity (ξ value) is comparable to the relative velocity of the flow structures. Therefore, figure 11(*b*) reveals the structures present within the turbulent boundary layer that are moving at the same speed as those structures within the turbulent spot.

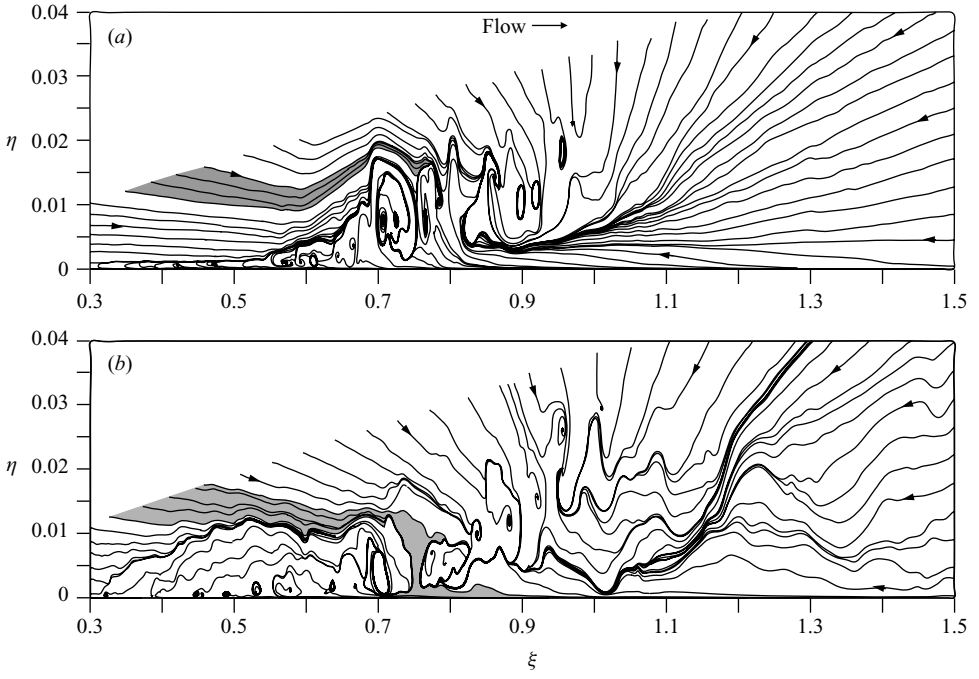

FIGURE 11. Similarity coordinate streamlines for Case 3 turbulent spot (*a*) and the turbulent boundary layer (*b*). The shaded areas represent a stream tube cross-section.

To highlight the process of entrainment for the turbulent spot in figure 11(*a*), a region of flow lying between a set of streamlines is shaded in grey. The convergence of this flow region as it impinges on the spot body shows that although free-stream fluid is entrained by the body of the spot, the fluid does not penetrate downward to the wall within the measurement plane. Although the cooler free-stream fluid may ultimately reach the surface owing to three-dimensional effects, it will almost certainly first mix with the warm fluid within the body of the spot, mediating the surface heat transfer. In contrast, a fluid packet from a similar free-stream location is shown in figure 11(*b*) for the turbulent boundary layer. In this case, the fluid moves directly to the wall, which will stimulate an increase in local surface-heat transfer.

Although caution is warranted in drawing conclusions from these instantaneous streamlines, they are reasonable evidence that the large-scale flow topology within a turbulent spot is fundamentally different from that within a turbulent boundary layer.

8. Surface shear stress

To investigate the commensurate fluid dynamic interaction of the spot with the surface, the surface shear stress was established from the PIV data, using a three-point sloping difference formula to calculate the instantaneous derivative $\mathrm{d}u/\mathrm{d}y$ at the surface. The uncertainty of the shear stress calculated using this technique is estimated to be less than 7 % for the turbulent spot and 13 % for the turbulent boundary layer, based on comparisons to known velocity profiles and the PIV measurement uncertainty reported by Praisner *et al.* (2001).

Figure 12(*a*) shows the ensemble-averaged wall shear stress generated by a spot, as determined from a series of surface hot-film measurements for 500 spots (Mautner &

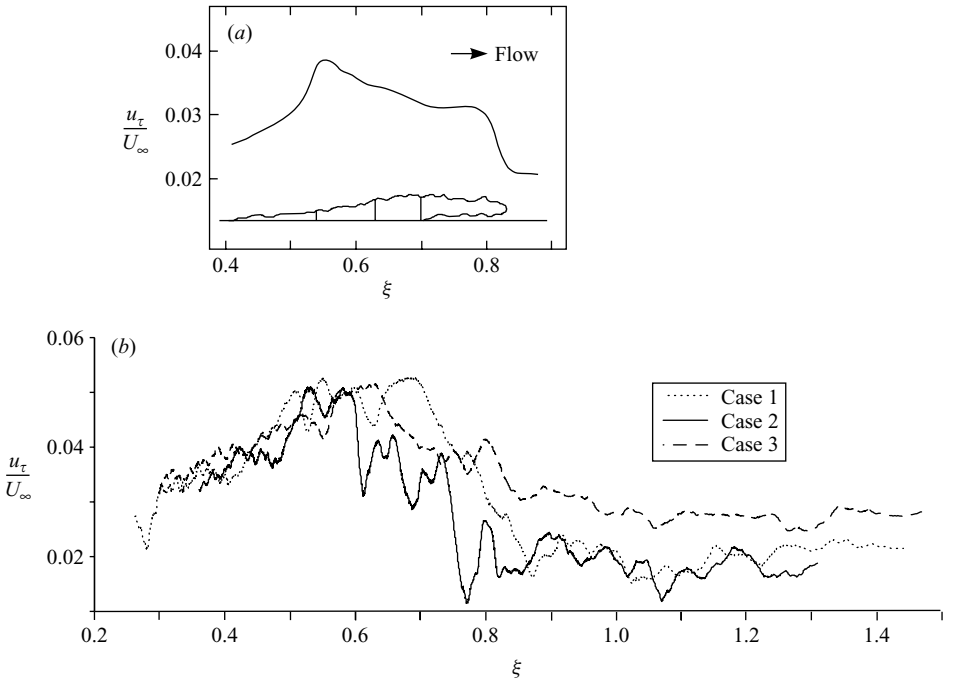

FIGURE 12. (*a*) Ensemble-average wall shear stress from Mautner & Van Atta (1986). (*b*) Moving average of surface wall stress for the present study calculated using PIV data.

Van Atta 1986). Here, the wall shear stress is presented in the form of shear velocity,

$$u_\tau = \sqrt{\frac{\tau_w}{\rho}}. \tag{8.1}$$

Included in the figure is Mautner & Van Atta's conjecture for the corresponding juxtaposition of the shear stress relative to the spot flow field. Figure 12(*b*) shows results obtained for the current study, plotted on matching scales for direct comparison. The shear stress for the three spot cases was filtered using a simple moving average to compare better the instantaneous data of the current study to the ensemble average of Mautner & Van Atta (1986). The trends are similar between figures 12(*a*) and 12(*b*), with the peak shear stress occurring in the range $0.5 < \xi < 0.6$. Similarly, the increase in shear stress associated with the leading edge of the spot occurs in the range $0.8 < \xi < 0.9$ in both figures 12(*a*) and 12(*b*).

It can be noted that Mautner & Van Atta (1986) suggest that the first sharp increase in shear stress occurs as a result of the passage of the leading-edge overhang of the spot. However, from the current study, the leading-edge overhang has already passed downstream by $\xi \approx 0.9$. The reason for the delayed response of the wall shear stress is that the structures comprising the overhang region are too far removed from the surface to influence the wall shear stress significantly, as was the case for the surface heat transfer. Additionally, a comparison with figure 9 shows that the region of maximum shear stress correlates with the incursion of high u velocity fluid near the trailing edge of the spot.

Despite matching the general features of the wall shear stress, the magnitude of the maximum scaled shear stress for all three cases of the current study is approximately 30 % higher than Mautner & Van Atta determined. This discrepancy may be explained

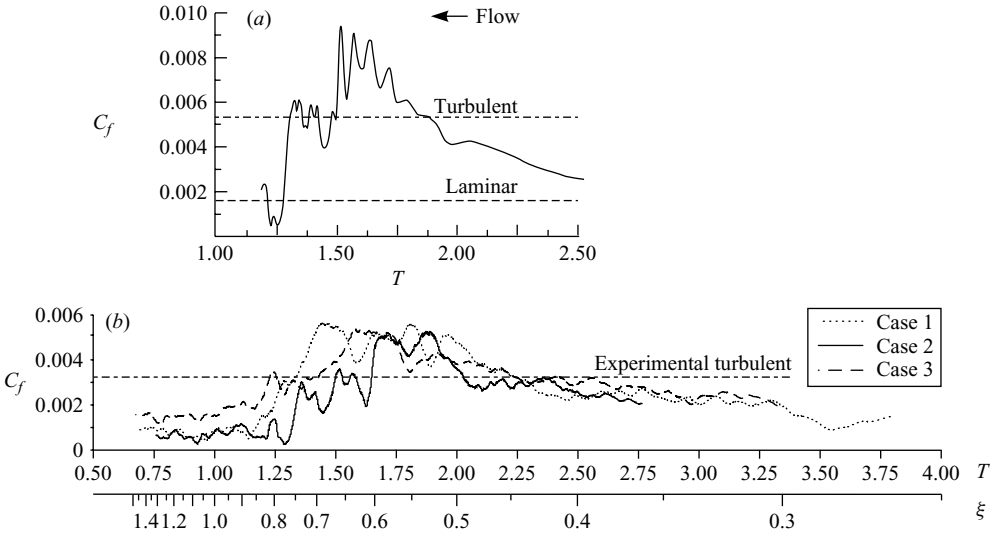

FIGURE 13. (*a*) Wall shear stress calculated by Singer (1996) at $(Re_{\delta^*})_i = 530$. (*b*) Moving average of surface wall stress calculated from PIV data from the present study.

by the fact that Mautner & Van Atta performed their experiments at a Reynolds number that is an order of magnitude larger than values of the current study, resulting in a thicker boundary layer and thus lower shear stress at the wall.

Figure 13(*a*) shows the wall shear stress for a young turbulent spot calculated by Singer (1996) using DNS. Singer originally presented the data using a surface friction coefficient, C_f, and dimensional time,

$$C_f = \frac{\tau_w}{\frac{1}{2}\rho U_\infty^2}. \tag{8.2}$$

In figure 13, Singer's plot has been rescaled using non-dimensional time, T, to allow a direct comparison with the current data. The similarity coordinate scale, ξ, is also shown for reference. As with figure 12, the general behaviour of the present results closely mirrors Singer's results. As was the case with the comparison to Mautner & Van Atta (1986), there is a difference in the magnitude of the shear stress. Here, we note that Singer's Reynolds number was lower than the current study, which may explain why Singer's C_f values are higher. For comparison, the average surface friction coefficient for the turbulent boundary layer examined in the present study is shown. Note that Case 3, which is obtained at the same free-stream velocity as the turbulent boundary layer, displays a maximum shear stress similar to the turbulent boundary layer, suggesting that the flow structures of the spot body have an effect on wall shear equivalent to the structures of the turbulent boundary layer.

Singer's data were calculated for $(Re_{\delta^*})_i = 530$, which is most similar to the Case 2 turbulent spot of the present study with $(Re_{\delta^*})_i = 568$. Notice in figure 13(*b*) that the shear stress pattern for Case 2 not only displays the general trend of Singer's results, but surprisingly many of the detailed features are remarkably similar. For example, in the region of $1.25 < \mathrm{T} < 1.50$, Singer's results (figure 13*a*) show two bimodal peaks in the shear stress. Two very similar bimodal peaks are also observed in the Case 2 data at a slightly later time.

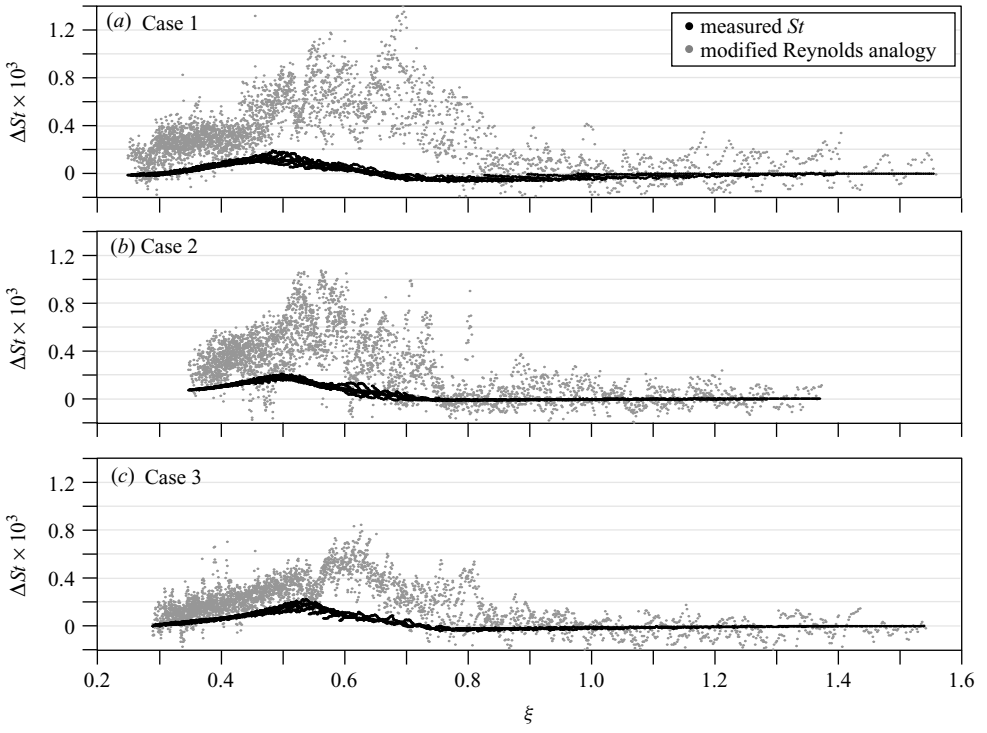

FIGURE 14. Comparison of experimentally determined and Reynolds-analogy-predicted Stanton number.

Given these results, it is of interest to understand how the surface shear stress is related to the measured surface heat transfer. For comparison, the modified Reynolds analogy is used to present the surface shear stress in the form of a Stanton number,

$$St = \frac{C_f}{2} Pr^{-2/3}. \tag{8.3}$$

Figure 14 compares the Stanton number determined from liquid crystal results with the Stanton number predicted from the modified Reynolds analogy (based on the wall shear stress obtained from the concurrent PIV results). The y-axis in figure 14 is the difference in the local Stanton number from the initial laminar-boundary-layer Stanton number. The difference is used because the Reynolds analogy is not directly applicable to the unheated starting-length case, and the initial laminar value of the Stanton number is not of primary importance to this comparison. The shear stress data (i.e. C_f) is not filtered, as was done previously. Although this introduces data scatter, in each case it is possible to identify a peak in the predicted Stanton number relative to a peak in the measured Stanton number.

Figure 14 suggests that for all three cases, the Reynolds analogy predicts an increase in Stanton number earlier in the spot cycle, and of a greater magnitude than is actually measured directly. The implication is that sufficient momentum exchange (reflected by the shear levels) takes place at the wall within the spot to facilitate a comparable increase in heat transfer. However, the failure of the measured Stanton number to follow the Reynolds analogy suggests that the fluid within the spot must not have the requisite temperature difference required to drive the heat transfer. This supports our

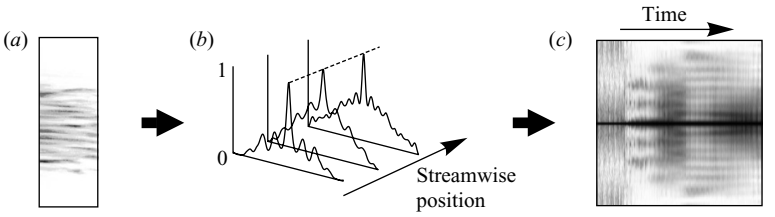

FIGURE 15. Data-processing steps used to quantify Stanton-number streak spacing. (*a*) Stanton-number data cropped to maximum spot width. (*b*) Normalized autocorrelations calculated for each streamwise location in a single Stanton-number frame. (*c*) All of the autocorrelations assembled into a single temporal sequence.

hypothesis that the body of the spot carries warm fluid that was previously entrained from the surface and is not able to mix effectively with the outer region flow.

9. Surface streak spacing

A final quantitative comparison that can be made between the spot and the turbulent boundary layer involves the surface-heat-transfer streak spacing. As discussed in § 5, the Stanton-number patterns generated by the turbulent spots were observed to display a somewhat organized pattern of streamwise streaks. These streaky patterns appear markedly similar to the low-speed streaks that are characteristic of the near-wall region of a turbulent boundary layer (Smith & Metzler 1983). To establish the lateral scale of the streak spacing for both the turbulent spot and the turbulent boundary-layer results, an autocorrelation function was applied to the instantaneous Stanton-number data.

Figure 15 illustrates the procedure for establishing the autocorrelations from the Stanton-number images. First, the Stanton-number data are cropped to the maximum width of the spot in the spanwise direction to reduce noise within the autocorrelation (figure 15*a*). An autocorrelation is then calculated for each streamwise location in the Stanton-number image (figure 15*b*). The dominant streak spacing of the Stanton number is represented by the distance between the primary centre peak and the next largest secondary peak within the autocorrelation. Because the spanwise spacing of the streaks is the focus of these plots, each autocorrelation is normalized to a unit scale of 0 to 1.0 to emphasize the change in the streak spacing as the spot passes. This process is repeated for each Stanton-number image to yield the streak spacing behaviour over the entire temporal record of the turbulent spot. The complete temporal sequence is shown as a contour plot with an inverted grey scale (peaks shown in black), with the primary autocorrelation peak along the centreline (figure 15*c*).

The temporal sequences for each spot case are shown in figure 16. The data are plotted versus non-dimensional time, T, to avoid compression of the data in the calmed region and more readily visualize the variation in the streak spacing pattern. The similarity coordinate scale is also shown for reference. Figure 16(*d*) shows the temporal streak spacing pattern for the turbulent boundary layer; the data were cropped to the same dimensions as for the Case 3 spot.

It is evident that each spot has three regions of different spacing patterns. The first pattern observed for $\xi > 0.7$ is characterized by the lack of any distinct streak spacing. This is the region in which the leading-edge overhang does not impact the surface heat transfer. The following pattern, in the range $0.5 < \xi < 0.7$, shows a relatively

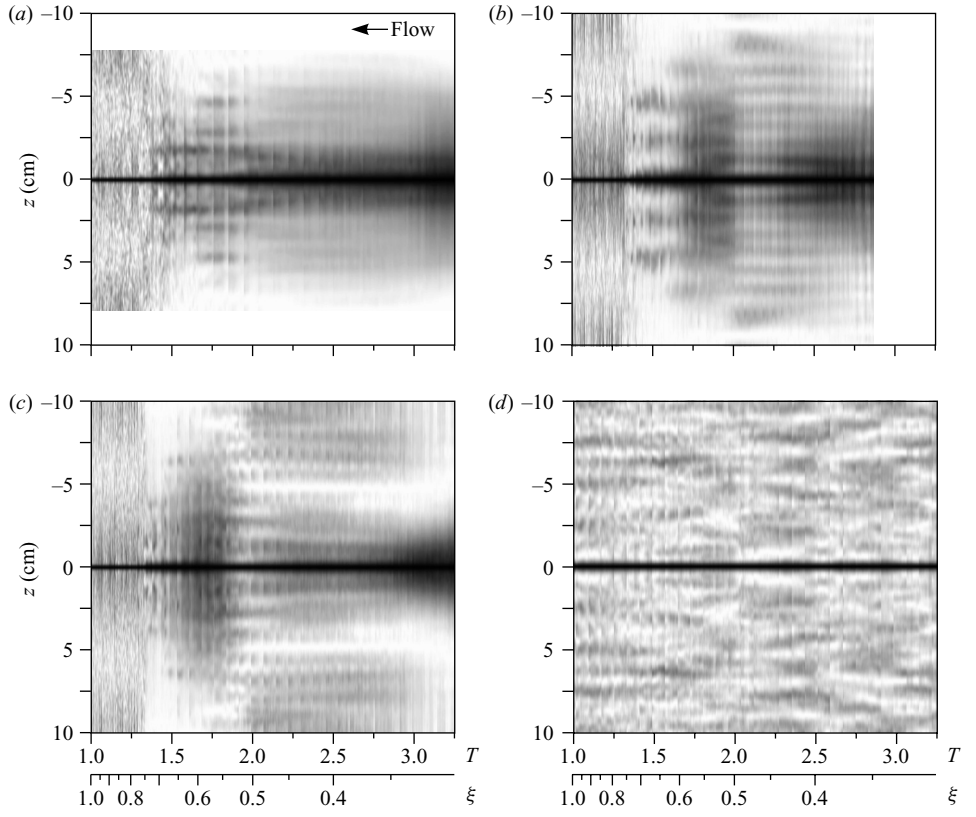

FIGURE 16. Normalized autocorrelation sequences for turbulent spots (*a–c*, Cases 1–3) and (*d*) turbulent boundary-layer heat-transfer patterns.

coarse spacing. The flow-field data shown in figure 9 indicate this is near the region where the body of the spot transitions to the trailing region. Finally, for $\xi < 0.5$, the narrowest streak spacing develops and this pattern persists for most of the remaining temporal record.

All three cases show that the spacing generally decreases as the spot passes. Comparing the spot behaviour to the patterns created by the low-speed streaks within the turbulent boundary layer (figure 16*d*) indicates that the turbulent low-speed streaks do not persist as long as the patterns in the trailing region of the spot. However, the temporal extent of the patterns of the low-speed streaks is most comparable to the spot patterns in the range $0.5 < \xi < 0.7$.

Since it is difficult to quantify the streak spacing from figure 16, a plot of the streak spacing, established with a peak-detection algorithm applied to the autocorrelation data, is shown in figure 17. Figure 17(*a*) shows the physical streak spacing, where the data are averaged using the same method as employed for developing figure 12, and cropped to include only those areas where a secondary autocorrelation peak could be accurately detected. For additional reference, it is noted that the streak spacing in figure 17(*a*) is in the range $1.0 < \lambda/\delta_L < 2.0$, where λ is the dimensional spacing of the streaks and δ_L is the average laminar boundary-layer thickness across the PIV field of view.

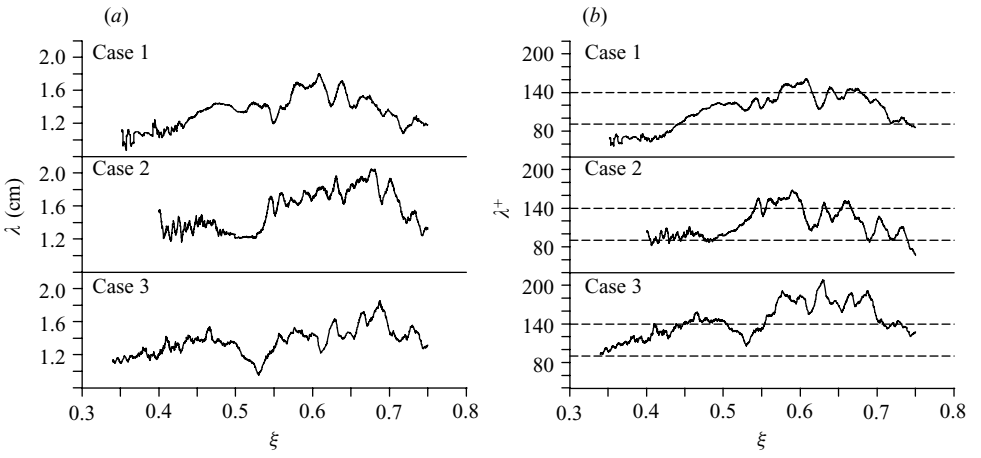

FIGURE 17. (*a*) Dimensional and (*b*) non-dimensional spanwise spacing of Stanton-number streaks for the three spot cases. The range of experimentally measured low-speed streak spacing for the turbulent boundary layer is shown as dashed lines.

A non-dimensional representation of the streak spacing is shown in figure 17(*b*) in the form of wall units,

$$\lambda^+ = \frac{\lambda u_\tau}{\nu}. \tag{9.1}$$

The shear velocity used to calculate the non-dimensional spacing was established from the averaged shear stress shown in figure 12. The TLC measurements provide a resolution better than 10 λ^+ units. The range of streak spacing for the turbulent boundary layer was determined to be $90 < \lambda^+ < 140$; this range is shown as dashed lines in figure 17(*b*).

Figures 17(*a*) and 17(*b*) both show that for all three spots the streak spacing initially increases, then decreases as the spot passes. The non-dimensional spacing shown in figure 17(*b*) clearly indicates that the turbulent spot streak spacing is generally comparable to the spacing of the patterns that result from the low-speed streaks within a turbulent boundary layer, in particular near the trailing edge ($\xi < 0.5$). It is hypothesized that this similarity in spacing indicates that the spots contain hairpin vortex packets (the source of the Stanton-number patterns) which are of similar scale and possibly strength to the packets observed within turbulent boundary layers.

10. Conclusions

The present study examined the instantaneous flow topology and surface heat transfer of three different turbulent spots with various levels of maturity. A modified set of similarity coordinates was used to compare spot characteristics and generate instantaneous streamline patterns to gain insight into the fluid dynamics within a spot. The combined data indicate that turbulent spots share key characteristics with turbulent boundary layers. The peak surface shear stress in turbulent spots is determined to meet or exceed average turbulent boundary-layer levels; surface heat transfer streak patterns are also found to be comparable in spanwise spacing. These results suggest that the strength and scale of the coherent structures within a turbulent spot can be comparable to those of a turbulent boundary layer. However, despite these similarities, a significant portion of the spot does not generate a measurable

increase in surface heat transfer above the laminar levels. In fact, the peak heat transfer occurs near the trailing edge of the spot as opposed to below the body of the spot, which appears to contain the largest and most energetic structures.

It is proposed that there are two reasons for the limited increase in heat transfer measured in the leading portion of a spot. First, the flow structures may not be in sufficient proximity to the surface to generate an appreciable increase in the surface heat transfer. This is most obvious at the leading-edge overhang, which is ineffectual in increasing either the heat transfer or shear stress at the surface. Secondly, streamlines indicate that the warm fluid from the heated surface is entrained into and confined within the body of the spot, reducing the temperature gradient with the surface and thus mitigating the surface heat transfer, even when there is energetic fluid exchange as indicated by the surface shear stress levels. The results of Antonia *et al.* (1981) and Chong & Zhong (2006) provide supporting evidence for this model, with their findings that the body of the spot is essentially comprised of relatively warm fluid.

At the trailing edge, Schröder & Kompenhans (2004) had previously identified the existence of hairpin vortex packets, and Antonia *et al.* (1981) and Chong & Zhong (2006) report that the calmed region is comprised entirely of fluid cooler than the laminar boundary layer. Synthesizing these findings with the current results implies that the higher-momentum fluid near the wall in the trailing region acts to thin the boundary layer and provide the near-wall hairpin structures with cooler fluid that is subsequently brought effectively to the surface to generate the highest heat transfer in the spot.

Although the present study examined spots at low Reynolds numbers, there is evidence that the general flow and heat transfer behaviour is characteristic of higher-Reynolds-number spots. The location of the peak heat transfer within the spot is consistent with findings of Clark *et al.* (1994) for transonic flows; however, the spots in the present study achieve only 80 % of the heat transfer of the higher-velocity spots (i.e. average turbulent boundary-layer levels). Because the magnitude of the peak heat transfer in the present study is consistent with previous turbulent spot measurements performed in a water channel by Zhong *et al.* (2000), it is possible that the difference in peak heat transfer is a Prandtl-number effect. In addition, as the present study determined that the relative change in heat transfer does increase with spot maturity, it is proposed that the magnitude of the heat transfer will eventually approach that of a fully turbulent boundary layer as the spot matures.

The authors wish to acknowledge the Air Force Office of Scientific Research for their support of this research. The advice and support of Paul Van Slooten at United Technologies Research Center is also greatly appreciated.

REFERENCES

Acarlar, M. S. & Smith, C. R. 1987 A study of hairpin vortices in a laminar boundary layer. Part 1. Hairpin vortices generated by hemisphere protuberance. *J. Fluid Mech.* **175**, 1–41.

Adrian, R. J. 1991 Particle-imaging techniques for experimental fluid mechanics. *Annu. Rev. Fluid Mech.* **23**, 261–304.

Adrian, R. J., Meinhart, C. D. & Tomkins, C. D. 2000 Vortex organization in the outer region of the turbulent boundary layer. *J. Fluid Mech.* **422**, 1–54.

Antonia, R. A., Chambers, A. J., Sokolov, M. & Van Atta, C. W. 1981 Simultaneous temperature and velocity measurements in the plan of symmetry of a transitional turbulent spot. *J. Fluid Mech.* **108**, 317–343.

Bowles, R. I., Davies, C. & Smith, F. T. 2003 On the spiking stages in deep transition and unsteady separation. *J. Engng Mech.* **45**, 227–245.

Brown, S. N. & Smith, F. T. 2005 Modelling the calmed region behind a spot. *Phil. Trans. R. Soc. Lond.* **363**, 1069–1078.

Cantwell, B., Coles, D. & Dimotakis, P. 1978 Structure and entrainment in the plane of symmetry of a turbulent spot. *J. Fluid Mech.* **87**, 641–672.

Ching, C. Y. & LaGraff, J. E. 1995 Measurement of turbulent spot convection rates in a transitional boundary layer. *Expl Therm. Fluid Sci.* **11**, 52–60.

Chong, T. P. & Zhong, S. 2006 On the momentum and thermal structures of turbulent spots in a favorable pressure gradient. *J. Turbomachinery* **128**, 689–698.

Clark, J. P., Jones, T. V. & LaGraff, J. E. 1994 On the propagation of naturally-occurring turbulent spots. *J. Engng Maths* **28**, 1–19.

Gad-El-Hak, M., Blackwelder, R. F. & Riley, J. J. 1981 On the growth of turbulent regions in laminar boundary layers. *J. Fluid Mech.* **110**, 73–95.

Gostelow, J. P., Walker, G. J., Solomon, W. J., Hong, G. & Melwani, N. 1997 Investigation of the calmed region behind a turbulent spot. *J. Turbomachinery* **119**, 802–809.

Gutmark, E. & Blackwelder, R. F. 1987 On the structure of a turbulent spot in a heated laminar boundary layer. *Exps. Fluids* **5**, 217–229.

Haidari, A. H. & Smith, C. R. 1994 The generation and regeneration of single hairpin vortices. *J. Fluid Mech.* **277**, 135–162.

Kim, H. T., Kline, S. J. & Reynolds, W. C. 1971 The production of turbulence near a smooth wall in a turbulent boundary layer. *J. Fluid Mech.* **50**, 133–160.

Krishnan, L. & Sandham, N. D. 2007 Strong interaction of a turbulent spot with a shock-induced separation bubble. *Phys. Fluids* **19**, 1–11.

de Lange, H. C., Hogendoorn, C. J. & Steenhoven, A. A. 1998 The similarity of turbulent spots in subsonic boundary layers. *Intl Commun. Heat Mass Transfer* **25**, 331–337.

Lin, J.-C. & Rockwell, D. 2001 Organized oscillations of initially turbulent flow past a cavity. *AIAA J.* **39**, 1139–1151.

Mautner, T. S. & Van Atta, C. W. 1986 Wall shear stress measurements in the plane of symmetry of a turbulent spot. *Exps. Fluids* **4**, 153–162.

Perry, A. E., Lim, T. T. & Teh, E. W. 1981 A visual study of turbulent spots. *J. Fluid Mech.* **104**, 387–405.

Praisner, T. J., Sabatino, D. R. & Smith, C. R. 2001 Simultaneously combined liquid crystal surface heat transfer and PIV flow-field measurements. *Exps. Fluids* **30**, 1–10.

Purtell, L. P., Klebanoff, P. S. & Buckley, F. T. 1981 Turbulent boundary layer at low Reynolds. *Phys. Fluids* **24**, 802–999.

Rockwell, D., Magness, C., Towfighi, J., Akin, O. & Corcoran, T. 1993 High image-density particle image velocimetry using laser scanning techniques. *Exps. Fluids* **14**, 181–192.

Sabatino, D. R. 1998 Instantaneous properties of a turbulent spot in a heated boundary layer. Master's thesis, Lehigh University.

Sabatino, D. R., Praisner, T. J. & Smith, C. R. 2001 A high-accuracy calibration technique for thermochromic liquid crystal temperature measurement. *Exps. Fluids* **28**, 497–505.

Sankaran, R., Sokolov, M. & Antonia, R. A. 1988 Substructures in a turbulent spot. *J. Fluid Mech.* **197**, 389–414.

Schröder, A. & Kompenhans, J. 2004 Investigation of a turbulent spot using multi-plan stereo particle image velocimetry. *Exps. Fluids* **36**, 82–90.

Singer, A. B. 1996 Characteristics of a young turbulent spot. *Phys. Fluids* **8**, 509–521.

Singer, A. B. & Joslin, R. D. 1994 Metamorphosis of a hairpin vortex into a young turbulent spot. *Phys. Fluids* **6**, 3724–3736.

Smith, C. R. 1996 Coherent flow structures in flat wall turbulent boundary layers: facts, mechanisms, speculation. In *Coherent Flow Structures in Open Channels.* (ed. P. J. Ashworth, J. L. Best, S. J. Bennet & S. J. McLelland), pp. 1–39. John Wiley.

Smith, C. R. & Metzler, S. P. 1983 Characteristics of low-speed streaks in the near-wall region of a turbulent boundary layer. *J. Fluid Mech.* **129**, 27–54.

Wygnanski, I., Sokolov, M. & Friedman, D. 1976 On a turbulent 'spot' in a laminar boundary layer. *J. Fluid Mech.* **78**, 785–819.

Wygnanski, I., Zilberman, M. & Haritonidis, J. H. 1982 On the spreading of a turbulent spot in the absence of a pressure gradient. *J. Fluid Mech.* **123**, 69–90.

Yaras, M. I. 2007 An experimental study of artificially-generated turbulent spots under strong favorable pressure gradients and freestream turbulence. *Trans ASME I: J. Fluids Engng* **129**, 563–572.

Zhong, S., Kittichaikan, C., Hodson, H. P. & Ireland, P. T. 1999 A study of unsteady wake-induced boundary-layer transition with thermochromic liquid crystals. *Proc. Instn Mech. Engrs* **213**, 163–171.

Zhong, S., Kittichaikan, C., Hodson, H. P. & Ireland, P. T. 2000 Visualization of turbulent spots under the influence of adverse pressure gradients. *Exps. Fluids* **28**, 385–393.